Electrochemical and optical studies of facile synthesized molybdenum disulphide (MoS$_2$) nano structures

Navpreet Kaur, Rameez Ahmad Mir, O.P. Pandey[*]

School of Physics and Materials Science, Thapar Institute of Engineering & Technology, Patiala, 147 004, India

A B S T R A C T

The global energy demand requires high energy conversion and storage devices. In order to enhance the utility of these devices, highly efficient, stable and cost effective catalyst and electrode materials are required. In the present study, the nano-size single phase molybdenum disulphide (MoS$_2$) has been synthesized at 700 °C via reduction-sulphurization method in a specially designed autoclave. The UV −Visible and photoluminescence results are in accordance with the Raman spectroscopy studies, confirming few layers (5—6 layers) of synthesized MoS$_2$ exhibiting a band gap of 2.29 eV. Based on structural and morphological results, the formation mechanism from MoO$_3$ to MoS$_2$ is proposed. The as-synthesized samples are expected to be promising stable catalyst for hydrogen evolution reaction (HER) through water splitting in both acidic and basic medium. The cyclic voltammetry (CV) test for 1000 cycles in basic medium shows enhanced stability of pure phase MoS$_2$. The electrochemical double layer capacitance (EDLC) of 2.8 mFcm^{-2} reveals that the synthesized material is a promising candidate for double layer capacitors and super-capacitors with high capacitance retention of 1000 CV cycles at fix scan rate.

© 2018 Elsevier B.V. All rights reserved.

1. Introduction

In the present era, focus is on the search of new materials such as transition metal dichalcogenides (TMDCs) owing to their potential applications in optical, thermal and electrical domains. The distinct unison of direct band gap, similarity to graphene, mono or few layer thickness, absence of dangling bond and supermagnetism phenomenon make TMDCs attracting candidates for industrial use [1—3]. Among chalcogens, transition metal sulphides (TMSs) are widely used for lubrication, catalysis, photoelectric devices and biomedical applications, because of the structural similarity with graphene [4—7]. They are known as beyond graphene materials as they overcome the limitations faced in the case of graphene owing to its chemical inertness and gapless semi-metallic nature. Moreover, they also exhibit unique electronic band structure for band-edge transitions [1,8—10].

Among different TMSs, molybdenum disulphide (MoS$_2$) having a layered structure of covalently bonded S-Mo-S units is mostly studied compound because of exceptional chemical, physical and optical properties [11]. It is a promising agent for novel diverse applications in the areas of electronics, optoelectronics, sensors and energy-storage devices [12—14]. MoS$_2$ is a structure dependent indirect and direct bandgap semiconductor and also shows interesting photoluminescence spectra depending upon the existing layers in the synthesized structure [15—17]. The potential use of MoS$_2$ in the field of catalysis has been well exploited. The similarity of MoS$_2$ with graphene widens its industrial use as catalyst for hydrogen production through water splitting and as electrode material for capacitors [11,18]. The layered structure of MoS$_2$ endows many properties, such as chemical stability, anisotropy, anti-photo corrosion and the unique property of band gap variation. These make it a promising low cost efficient catalyst and support for hydrogen evolution reaction (HER) via photocatalysis and electrocatalysis [19—22]. Most of the chemical properties depend directly on number and sequence of stacking pattern of MoS$_2$ layers. While reacting chemically, the metallic edge planes with the existence of sulphur vacancies appear as active sites, as they can accept or donate electrons and results in high activity and efficiency of MoS$_2$. Whereas, the sulphur atoms lying on basal planes behave as inert because they are completely coordinated [11]. The efficiency of water splitting through hydrogen evolution reaction (HER) is greatly influenced by surface characteristics and method of

* Corresponding author.
E-mail address: oppandey@thapar.edu (O.P. Pandey).

synthesis [23]. For efficient catalytic and capacitance applications, the synthesis of MoS_2 at nano scale with uniform sulphurization and controlled morphology is highly desirable. Till date, only limited reports are available on morphology controlled techniques.

The long duration multi step processes reported are costly and energy consuming. Most of the researchers have reported a hydrothermal method for synthesis of nano MoS_2 at low temperatures, but this technique fetches longer duration of holding time and multiple precursors [24–28]. Shomalian et al. [4] synthesized nano MoS_2 via the tedious prolonged technique of complex polymerization through sol-gel method using different precursors. Ravikumar et al. [29] have synthesized MoS_2 nanoflowers by hydrothermal route in 48 h. Analyzing these limitations, it is felt to reduce the synthesis time by adopting different synthesis route. To the best of our knowledge, only Afsar et al. [30] recently reported the single step synthesis of MoS_2 nanoflowers via liquid solid phase reaction technique at 650 °C for photocatalytic applications.

In the present work, synthesis of MoS_2 nano structures via concurrent reduction and sulphurization at 700 °C for 10 h reaction time is reported. The synthesized nano MoS_2 has been characterized and tested for its application as electrocatalyst for water splitting through HER and electrode material for electrochemical devices.

2. Experimental

2.1. Chemicals

In this study, the nanosize MoS_2 has been synthesized via reduction-sulphurization method using a specially designed autoclave [31]. High purity precursors of molybdenum and sulphur were used for synthesis. Molybdenum trioxide (MoO_3) (*Loba Chemie*) was used as molybdenum source and sodium sulphide (Na_2S) (*Loba Chemie*) was used as sulphur source, whereas magnesium (Mg) (*SDFC Ltd.*) acted as reducing agent. The detailed route followed for synthesis is discussed below:

2.2. Sample preparation

The precursor's molybdenum trioxide (MoO_3) and sodium sulphide (Na_2S) along with reducing agent (Mg) were mixed in agatemortar. Then, the solid mixture was transferred into the autoclave and sealed properly. The sealed autoclave was heated at a constant

2.3. Characterization

The as-prepared samples were characterized with the help of *PANALYTICAL X'PERT PRO* XRD diffractometer armed with X'Celerator solid state detector having nickel (Ni) as an inbuilt beta filter. The Cu-Kα radiations, generated from Cu anode target material with λ = 1.53333 Å, were used to detect phase and obtain the crystal structure of the samples. The morphology of the optimized samples in powder form was determined with the help of FESEM, using *HITACHI SU8010* instrument, operating at an accelerating voltage of 5 kV. The below atomic level properties of ultra-thin samples were investigated using HRTEM by *JEOL 2100* operating at a voltage of 200 kV to record TEM micrographs at various magnifications. The layered structure was investigated via Raman spectroscopy model *Renishaw* with 514 nm laser light. UV−Visible reflectance spectra were carried out at room temperature with *Hitachi U3900H spectrophotometer* in the spectral range of 200−800 nm to study optical properties and estimate the band gap. The photoluminescence (PL) spectra were recorded on *Agilent Technologies* Model *Cary Ellipse* equipment with Xenon lamp. The surface composition and bonding states were investigated by X-ray photoelectron spectroscopy (XPS) using *PHI 5000 Versa Prob II, FEI Inc.* via means of Al K_α radiation (1486.7 eV, Ag standard).

2.4. Calculation methods and formulas applied

The Scherrer equation states the relation between Bragg peak position (2θ) and crystallite size (D) as [32]:

$$D = \frac{k\lambda}{\beta cos\theta} \tag{1}$$

Here, D stands for calculated crystallite size, k is shape factor (0.9393), λ corresponds to the wavelength of Cu Kα radiation (0.154 nm) and θ is Bragg's angle. β used in the above equation refers to Bragg's peak breadth, which is an amalgamation of both sample and instrumental dependent effects. The instrumental peak broadening was obtained with the help of Si standard sample and was then subtracted from observed value, so that:

$$\beta = \left\{ \left(\beta_{observed}^2 \right) - \left(\beta_{instrumental}^2 \right) \right\} \tag{2}$$

Young's modulus ($E_{(hkl)}$) of the hexagonal structure along the best-fit plane: [33].

$$E_{(hkl)} = \frac{\left[h^2 + \frac{(h+2k)^2}{3} + \left(\frac{a}{c} l \right)^2 \right]^2}{S_{11} \left(h^2 + \frac{(h+2k)^2}{3} \right)^2 + S_{33} \left(\frac{a}{c} l \right)^3 + (S_{33} + 2S_{13}) \left(h^2 + \frac{(h+2k)^2}{3} \right) \left(\left(\frac{a}{c} l \right)^2 \right)} \tag{3}$$

heating rate of 5 °C/min in furnace upto required temperatures (300, 300, 500, 600, 700, 800 °C) for distinct holding times (8, 10, 12, 15 h). Optimization in quantities of precursors, temperature and time were done to obtain pure phase MoS_2. The synthesized powder so obtained was washed with diluted hydrochloric acid (2:1) to remove MgO/Mg followed by washing with distilled water and drying at 100 °C for 12 h in an oven. The route followed for synthesis of nano MoS_2 is schematically represented in Fig. S1 (SI, supplementary information) and the variation in synthesis conditions have been listed in Table 1.

Where, S_{11}, S_{33}, S_{33} and S_{13} all are elastic compliances found by using values of elastic constants for MoS_2 hexagonal system [34].

The stress and strain were calculated via Williamson-Hall analysis are:

$$Strain\ (\varepsilon) = \frac{\beta_{hkl}}{4tan\theta} \tag{4}$$

$$Stress\ (\sigma) = Y\varepsilon \tag{5}$$

Kubelka-Munk equation states [35]:

Table 1
Optimization in synthesis conditions.

Sample Id	MoO$_3$ (g)	Mg (g)	Na$_2$S·3H$_2$O (g)	Temperature (°C)	Holding time (hrs)
MS-1	1.339	2.5	2	300	10
MS-2	1.339	2.5	2	500	10
MS-3	1.339	2.5	2	600	10
MS-3	1.339	2.5	2	700	10
MS-5	1.339	2.5	2	800	10
MS-6	1.339	2.5	2	500	12
MS-7	1.339	2.5	2	500	15
MS-8	1.339	2.5	3	600	10
MS-9	1.339	2.5	3	700	10
MS-10	1.339	2.5	3	700	12
MS-11	1.339	2.5	3.5	700	10
MS-12	1.339	2.5	4	700	10
MS-13	1.339	2.5	4.5	700	10
MS-14	1.339	2.5	3.5	700	8

$$[F(R)\cdot h\nu]^n = A(h\nu - E_g) \tag{6}$$

Where A is proportionality constant, ν refers to frequency and E_g obtained is band gap and F(R) is reflectance.

2.5. Electrochemical measurements

The as-prepared samples were investigated for their electro-catalytic activity test using *Bio-logic EC Lab SP300* standard setup. Out of the three electrodes in the system; platinum was used as the counter electrode, whereas the working electrode was prepared manually. For fabrication of working electrode, 0.1 mg of carbon black was added to 1 mg of MS-11 (MoS$_2$) and MS-13 sample, which was mixed in 250 µL of ethanol and the solution was sonicated for 25 min to achieve uniform dispersion of particles. The top of glassy carbon electrode (GCE), which has the surface area of 0.070 cm^2, was drop-casted by 10 µL of the above dispersed solution. A single drop of Nafion 117 solution (Sigma Aldrich) from 10 µL was put onto the GCE top and was dried overnight.

The measurements were done using reversible hydrogen electrode (RHE) as the reference electrode in the 0.5M H$_2$SO$_4$ electrolyte solution. Saturated calomel electrode (SCE) was used as the reference for measurements when alkaline (0.5M KOH) was used as the electrolyte. All the measurements were then used in RHE, as SCE measurements were converted using eq. (7)

$$RHE = V_{SCE} + 0.059 \times pH + 0.243 \tag{7}$$

Where V_{SCE} is the voltage with respect to SCE.

3. Results and discussion

The effects of synthesis parameters on the formation of MoS$_2$ nanoparticles were studied in the present work. In the initial set of experiments, the mixture of MoO$_3$ (1.339 g), Mg (2.5 g) and Na$_2$S (2 g) was taken into an autoclave at different temperatures for 10 h. However, in the next set of experiments heating duration and sulphur content was varied.

3.1. X-ray diffraction (XRD) analysis

XRD data was analyzed using X'Pert HighScore Plus software by matching the data peaks with reference International Centre for Diffraction Data (ICDD) reference patterns.

3.1.1. Effect of reaction temperature on the synthesis of MoS$_2$ nanostructures

Fig. 1 (a) shows the XRD patterns of samples synthesized at different temperatures varying from 300 °C to 800 °C with fixed a holding time of 10 h. MS-1 shows the formation of a major peak of MoS$_2$ along with peaks of molybdenum dioxide (MoO$_2$) and molybdenum (III) sulphide (Mo$_2$S$_3$). The MS-2 shows the formation of MoS$_2$ and MoO$_2$. No other impure phases as Mo$_2$S$_3$ were observed in MS-2. The formation of MoO$_2$ phase reveals that the temperature (300 °C and 500 °C) was not sufficient for sulphurization of reduced molybdenum dioxide phase. Therefore, the temperature was increased even further, favoring the reduction of MoO$_3$. At higher temperatures, (600 °C, 700 °C, 800 °C) formation of molybdenum metal dominated, as only small peaks of MoS$_2$ were observed. The impurity phase (Mo) present at high temperatures revealed lack of sulphur source, even if the reduction process of MoO$_3$ to Mo metal has been accomplished. The formation of Mo metal at higher temperatures reveals the fast reduction of MoO$_3$/MoO$_2$ to Mo metal without the proper sulphurization.

3.1.2. Effect of holding time at a particular temperature on the synthesis of MoS$_2$ nanostructures

In Fig. 1 (b), the X-ray diffractograms of samples synthesized at 500 °C with variation in holding times of 10, 12 and 15 h is shown. The major peak corresponding to MoS$_2$ at $2\theta = 14.398$ remained constant in all three samples, whereas the variations in impure phases were observed. When the time was increased to 12 h (MS-6), the phase formation of Mo metal, MoO$_2$ and even some peaks of MoO$_3$ were observed, suggesting reverse oxidation of formed phase to MoO$_3$. Further increase in time upto 15 h showed the dominance of MoO$_3$ peaks indicating that MoO$_2$ phase has transformed into MoO$_3$ with the increase in reaction time at fixed temperature. The reforming of MoO$_3$ could be attributed to the competition between oxygen and sulphur because of their atomic sizes. Both the oxygen and sulphur belong to the same group and oxygen being smaller gets bonded easily as compared to sulphur. The results with the increase in time were not satisfactory, furthermore optimization was introduced in other parameters. Afsar et al. [30] in 2018 synthesized MoS$_2$ at the higher temperature (650 °C) by liquid-solid phase reaction method. Therefore, the optimization was done at relatively higher temperatures. As observed from Fig. 1 (a), the reduction was complete at 600 °C and 700 °C, but sulphurization was found to be minimal; so addition in sulphur source was done in further experiments.

3.1.3. Effect of sulphur source on the synthesis of MoS$_2$ nanostructures

The sulphur content was increased from 2 g to 3 g at 600 °C (MS-8) and 700 °C (MS-9) to enhance the sulphurization process. The XRD patterns shown in Fig. 1 (c) suggest that at 600 °C (MS-8) only a small peak of MoS$_2$ appeared along with impure phases of Mo, MoO$_2$ and Mo$_8$O$_{23}$. But at 700 °C (MS-9) MoS$_2$ phase dominated, with the presence of a small single peak of Mo and Mo$_2$S$_3$ phases. The variation in sulphur content affects the formation of MoO$_3$ to MoS$_2$ as predicted in Mo and S phase diagram [36]. The reaction temperature 700 °C revealed that the reduction and sulphurization of MoO$_3$ was almost accomplished. Further, to remove the impurities (Mo, Mo$_2$S$_3$) however, very small in MS-9, the holding time was increased to 12 h (MS-10 as shown in Fig. 1 (d)).

In the sample MS-10 (holding time of 12 h), the impure phases as Mo$_2$S$_3$, Mo and MoO$_3$ along with major phase Mo were obtained. Here, also MoO$_3$ was obtained when holding time exceeded 10 h. This could be the result of reverse oxidation of the formed MoS$_2$ because of the difference in atomic sizes of oxygen and sulphur. There is always a rivalry in both of them to bond with other atoms
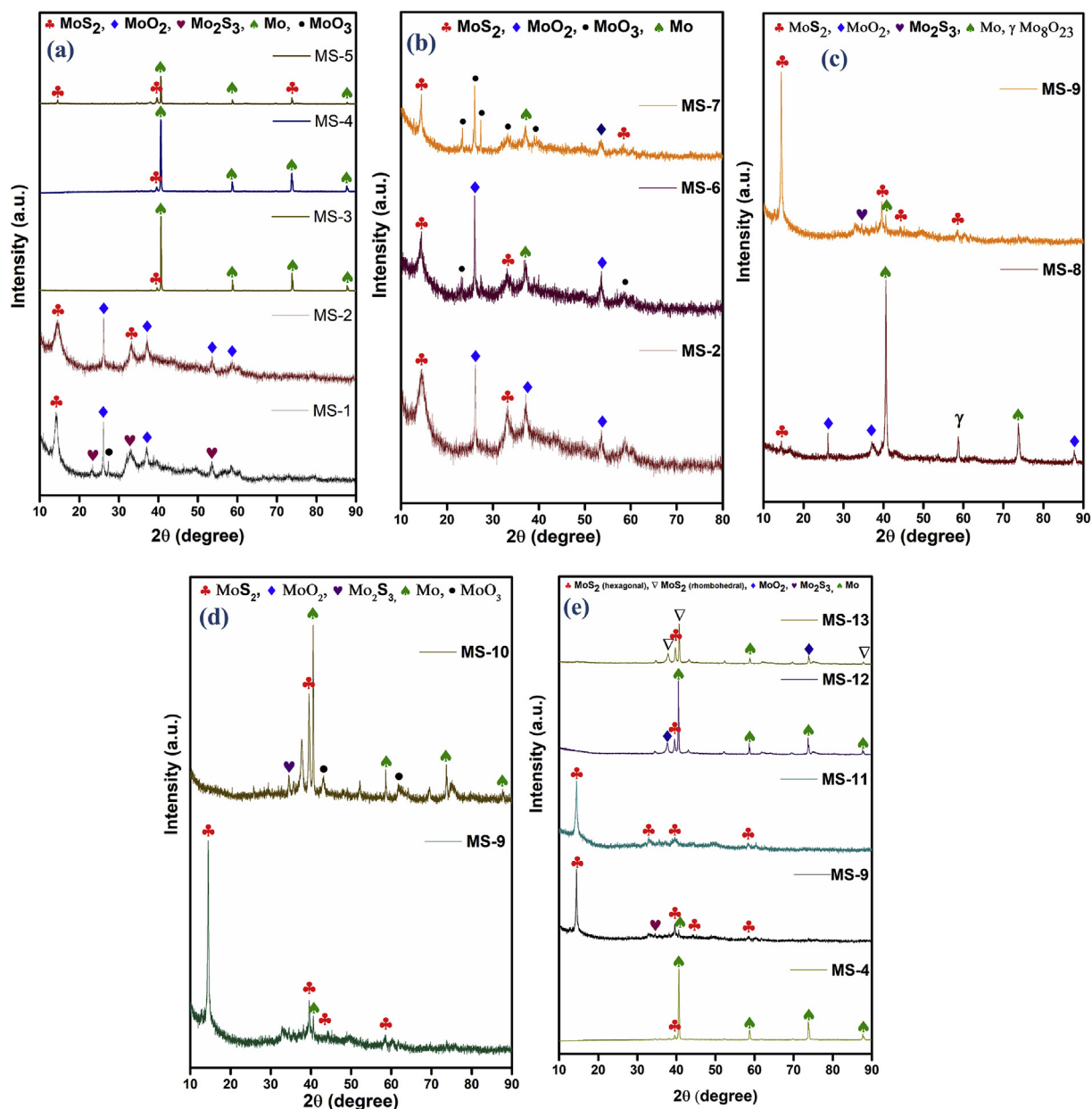
Fig. 1. **(a)** X-ray diffractograms of samples synthesized at 300 °C (MS-1), 500 °C (MS-2), 600 °C (MS-3), 700 °C (MS-3), and 800 °C (MS-5), **(b)** XRD patterns of samples heated for different holding times for 10 h (MS-2), 12 h (MS-6), 15 h (MS-7), **(c)** Effect of increase in sulphur source at 600 °C (MS-8) and 700 °C (MS-9), **(d)** Effect of holding time for 10 h (MS-9) and 12 h (MS-10) at 700 °C temperature and **(e)** Effects of variation in sulphur source; 2 g (MS-3), 3 g (MS-9), 3.5 g (MS-11), 3 g (MS-12) and 3.5 g (MS-13).

but oxygen having the advantage of smaller size replaces sulphur easily at relatively higher temperatures.

Fig. 1 (e) shows typical XRD patterns of samples synthesized with variation in sulphur content; 2 g (MS-3), 3 g (MS-9), 3.5 g (MS-11), 4 g (MS-12) and 4.5 g (MS-13) at the fixed temperature of 700 °C and holding time of 10 h. The patterns in MS-9 (3 g) showed sulphurization has been accomplished to a greater extent, but small impure intermediate phases of Mo_2S_3 and Mo metal has been detected. In an attempt to attain complete sulphurization, sulphur content was increased upto 3.5 g in sample MS-11, which resulted in pure phase of MoS_2. This increase in sulphur content resulted in the proceeding of reaction in the forward direction. The major peak grown at $2\theta = 14.398$ and very small humps at higher 2θ values confirmed the synthesis of nano MoS_2. The results indicated that the as-prepared sample has amorphous nature and layers were

weakly stacked [37,38]. Increasing the sulphur content to 4 g (MS-12) shows the reverse effect of Mo formation, which could be the result of pressure generated with higher sulphur content. The transformation in crystal structure for MoS_2 (hexagonal) to MoS_2 (rhombohedral) was observed in MS-13 having sulphur content of 4.5 g, which is because of pressure effect generated due to excess sulphur content [39]. Decreasing the holding time at 700 °C to 8 h (sample MS-14 as shown in Fig. S2 (SI)) also shows the presence of some oxide phases and intermediate Mo_2S_3 phases, which reveals sulphurization reaction has not accomplished at this stage. The hexagonal MoS_2 has been synthesized in MS-11 (ICDD card reference code: 03-065-7025), whereas the MoS_2 synthesized with higher sulphur content (4.5 g) in MS-13 exhibited rhombohedral structure (ICDD card reference code: 01-073-0932), which exists at relatively higher pressure [11,40]. The results show variation in

Table 2
Crystallite size, stress and strain analysis of MS-11 using Scherrer formula.

Sample Id	2θ	D (nm)	Young's modulus (TPa)	Strain (×10⁻⁴)	Stress (MPa)
MS-11	14.398	19.39277	0.3	1.24	49

reaction kinetics due to the effect of pressure produced inside the autoclave when sulphur content is increased. The optimized condition to get single phase nano crystalline phase for MS-11 was 700 °C with sulphur content of 3.5 grams and holding time of 10 h.

3.2. Crystallite size of single phase molybdenum disulphide

The XRD patterns are useful in determining the crystallite size and lattice parameters. Pearson VII peak function was used for curve fitting of major peak (002) in XRD pattern of pure phase MoS_2 (MS-11). Scherrer formula, which is volume weighted quantity, was then taken in account for the calculation of crystallite size. The crystallite size of single phase MoS_2 was calculated to be 19.39 nanometers as given in Table 2.

3.2.1. Young's modulus, stress and strain analysis

To understand the elastic properties, Young's modulus for this hexagonal structure was calculated, which resulted to be 0.3 TPa. The results are in good agreement with earlier reported literature [41]. Table 2 shows the value of Young's modulus, strain and stress as calculated for MS-11 corresponding to the major peak (002).

3.3. Field emission scanning electron microscopy (FESEM) analysis

The morphological characteristics of the sample having a single phase were studied by FESEM analysis. Fig. 2 (a & b) shows the micrographs of sample MS-11, synthesized at 700 °C with holding time of 10 h. The FESEM micrographs at different magnifications show that the particles are highly agglomerated. The results also confirm homogenous spherical/faceted morphology of particles.

3.4. High-resolution transmission electron microscopy (HRTEM) analysis

Fig. 3(a–d) shows the transmission electron microscopy (TEM) and HRTEM micrographs of as-synthesized nano MoS_2 particles. The TEM micrographs Fig. 3 (a & b) reveal the agglomeration and preferential growth of nanolayered structures. The results are in agreement with the XRD results. Certain particles in Fig. 3 (c) are agglomerated and possess faceted like shape which indicates

resemblance to graphene and formation of nanoflakes. The HRTEM in Fig. 3 (d) reveals the lattice fringes of 0.327 nm corresponding to (003) plane having similar d-spacing as MoS_2 (ICDD card: 03-0665-7025). The HRTEM micrographs in Fig. 3 (d) confirms pure phase hexagonal MoS_2 consistent with XRD results. The particle size distribution calculated at various scan areas is shown in the inset of Fig. 3(c), which shows an average particle size of 70 nm.

3.5. Raman spectroscopy

Raman spectroscopy, a non-destructive powerful characterization technique, was performed to analyze the layered structure of as-prepared MoS_2 nanostructures in terms of Raman active modes [42]. The measurements of Raman spectroscopy were performed with excitation laser of 514 nm. Fig. 4 reveals two Raman active modes; one in-plane (E_{2g}) mode at 384 cm⁻¹ and an out-of plane mode (A_{1g}) at 409 cm⁻¹. Here, the E_{2g} mode indicates opposite in plane vibrations of Mo and S atoms, whereas the A_{1g} mode corresponds to out of plane S atom vibrations [43]. As per the dependence of these modes on sample thickness, the decrease in former mode and increase in latter with sample thickness has been well established. The energy difference between both modes as shown in Fig. 4 was found to be 25 cm⁻¹, corresponding to the existence of 5–6 layers as per reported literature [44]. This shift in frequency modes owed to the phenomenon of Coulombic interaction and possible alteration in intralayer bonding [44].

3.6. UV–Visible analysis

UV–Vis reflectance spectroscopy was performed to analyze optical properties and estimate band gap energy of prepared MoS_2 sample. Fig. 5 (a) shows reflectance spectra recorded in the wavelength range of 200–800 nm at room temperature. As the spectroscopy data was recorded for reflectance against UV–Vis rays, the Kubelka-Munk function was used to find the band gap energy. The band gap of MoS_2 depends on its structure and morphology. In the analysis of MS-11 the plot between energy (hν) on X-axis vs $[F(R)\cdot h\nu]^n$ on Y-axis, where n is ½, is plotted. Fig. 5 (b) shows a direct band gap of 2.29 eV. This blue shift in band gap energy could be attributed to the additional quantum confinement of Z-direction in as synthesized hexagonal MoS_2 [45].

3.7. Photoluminescence

Fig. 6 represents the emission spectra of as-prepared MoS_2 nano structures (MS-11). The emission spectra of as-synthesized sample was recorded in the range of 400–800 nm under the UV excitation of 237 nm. With the reduction in sample thickness, the d orbitals of
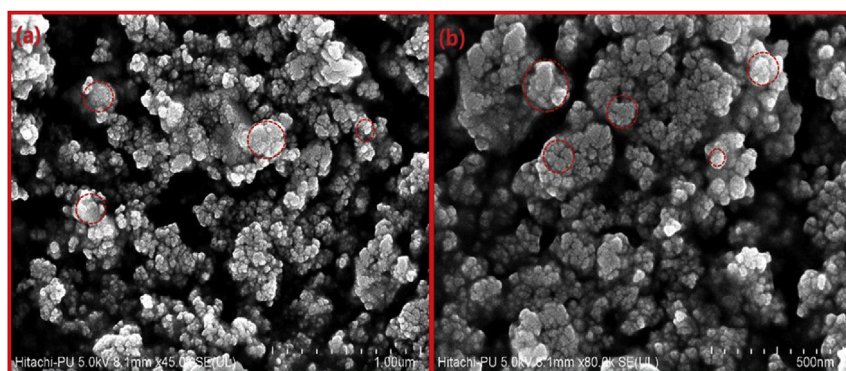

Fig. 2. FESEM micrograph of sample MS-11 with **(a)** 1 μm magnification **(b)** 500 nm magnification.
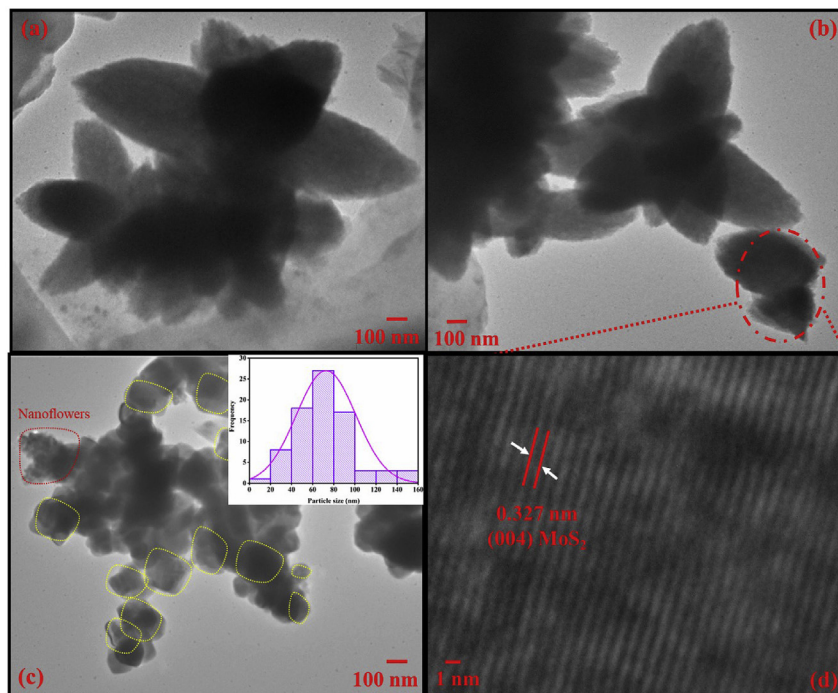
Fig. 3. TEM micrographs of MS-11 sample; **(a)** and **(b)** shows nano-flower morphology, (c) shows agglomeration of particles (inset image shows particle distribution as obtained from different scan areas of TEM images), (d) HRTEM micrograph showing lattice fringing of sample MS-11.

Mo atoms and p_z orbitals of S atoms hybridize, giving rise to photoluminescence phenomenon [46]. In Fig. 6, the emission peak observed at 417 nm and a broad hump centered at 446 nm corresponds to blue luminescence, while peaks observed at 483 nm and 532 nm corresponds to green luminescence. The peak intensity at 483 nm was found to be prominent in comparison to other peaks. This revealed that as-synthesized nano structures emitted blue color as the dominant peak lies in the blue region, when excited in UV-region. According to the reported literature, the peaks of MoS_2 PL spectra emerges around 670 nm and 627 nm, corresponding to A1 and B1 direct excitonic transitions [16]. But, in the as-prepared sample, the peaks were absent implying that the sample thickness was higher than 7.6 nm, as suggested by Eda et al. in 2011 [47].
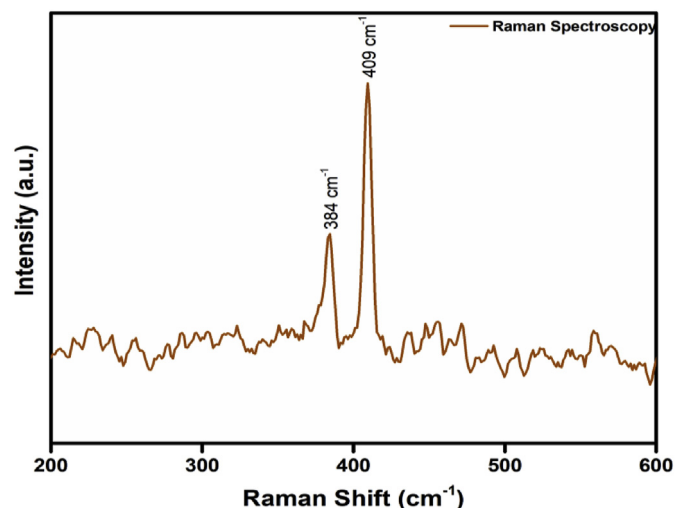
Fig. 4. Raman spectra of MS-11.

3.8. X-ray photoelectron spectroscopy

The surface chemistry, composition and bonding states of different elements were investigated by X-ray photoelectron spectroscopy (XPS) via peak deconvolution. Survey spectra of MS-11 sample is represented in Fig. 7 (a) exhibiting peaks at 160, 228, 282, 396, 411 and 532 eV referring to S2p, Mo3d, C1s, Mo3p, Mo3p and O1s, respectively. The peaks were with respect to standard carbon peak (located at 282 eV) taken as reference. The high resolution (HR) spectra of Mo3d (Fig. 7 (b)) shows two peaks at 229.9 eV and 231.79 eV in regards to Mo $3d_{3/2}$ and Mo $3d_{1/2}$ indicating presence of Mo^{4+} in the as-synthesized MoS_2. The peak situated at lower binding energy of 227.1 eV attributed to S2s peak of MoS_2 [48]. The XPS confirmed the formation of MoS_2 in the synthesized samples. A parallel set of peaks at 235.00 eV and 232.18 eV were detected which were assigned to (Mo^{+6}) $Mo3d_{3/2}$ and $Mo3d_{5/2}$, respectively [32]. Both of these peaks appeared due to oxidation of sample exposed to air during XPS analysis. The two peaks at 161.23 eV and 163.965 eV occurring in HR spectra of S2p in Fig. 7 (c) were attributed to $2p_{3/2}$ and $2p_{1/2}$ in MoS_2, whereas another peak occurring at 162.633 eV also corresponded to 2p according to XPS NIST database [49].

3.9. Formation mechanism of MoS_2

The mechanism for the formation of MoS_2 has been proposed on the basis of XRD results and morphological features and its pictorial representation is shown in Fig. 8. Mg, along with precursors is added to enhance reduction and favors the fast reaction in the forward direction. As per reported literature, MgO catalyst is formed via interaction of Mg and oxygen present in the autoclave [32]. Then, the reduction of precursors is bought out by MgO to form H_2 and H_2S gases. Both these gases are supposed to help in reducing MoO_3 to MoO_2, owing to their diffusion coefficient [50,51]. At the same time, smaller size hydrogen enters the grain
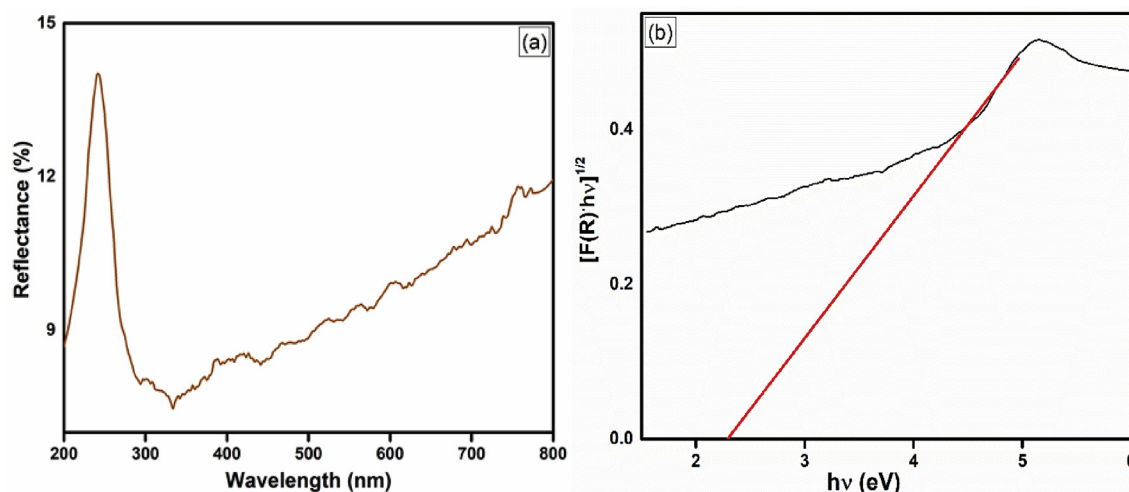
Fig. 5. (a) Reflectance spectra of sample MS-11, (b) Corresponding $[F(R)\cdot h\nu]^n \sim h\nu$ curves of sample MS-11 direct band gap.
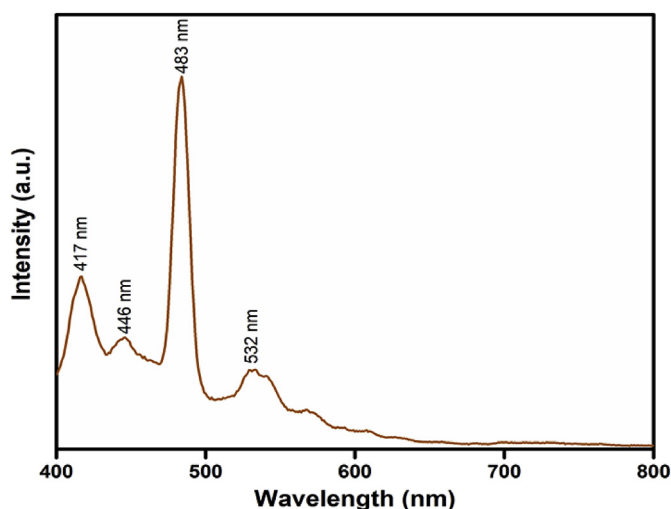

Fig. 6. Photoluminescence spectra of sample MS-11.

boundaries of oxides; fragmenting them into smaller particles. Sulphur present in the system is engaged in enclosing the newly produced particles.

As shown in Fig. 1, in all the samples synthesized in the temperature range 300—500 °C, the reduction of MoO_3 and simultaneous sulphurization resulted in the formation of MoO_2, MoS_2 and

Mo_2S_3. Moreover, almost identical diffraction patterns have been obtained with varying intensities. All possible reaction paths taking place inside the autoclave are listed in SI (Equations S1 to S26). The most feasible reaction for temperature 300—500 °C is written in equation (8).

$$5MoO_3 + 6Mg + 5Na_2S\cdot 3H_2O \rightarrow MoS_2 + MoO_2 + Mo_2S_3 + MoO_3$$
$$+ 10NaOH + 6MgO + H_2 + 9H_2O$$

(8)
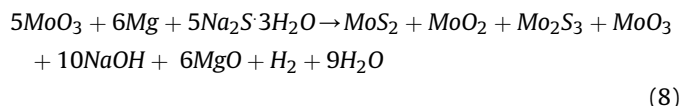
The graph between the heat of formation (ΔH) and temperature (K) for equation (8) has been plotted in Fig. 9. The other possible reaction paths taking place in the said temperature range are given in equations S1-S6 (SI). The variation of ΔH with temperature for the corresponding reactions is given in Fig. S3 (SI). The only reactions having negative values of ΔH are considered as feasible reactions. As per information given in equations S1-S6 and Fig. S3 (SI), it can be concluded that among feasible reactions only one reaction that takes place above 1000 K is possible one. This indicates that along with temperature, the pressure generated in the autoclave played the key role in the reduction of MoO_3. So, the effect of pressure along with temperature has resulted in the formation of these intermediate compounds.

However, as per reported literature, MoO_3 gets reduced to MoO_2 at the initial stages, along with the evolution of some gases [52]. Fig. 9 depicts the relationship between the heat of formation (ΔH) and temperature (in Kelvin) for the most possible reaction (9) for reduction of MoO_3 to MoO_2.
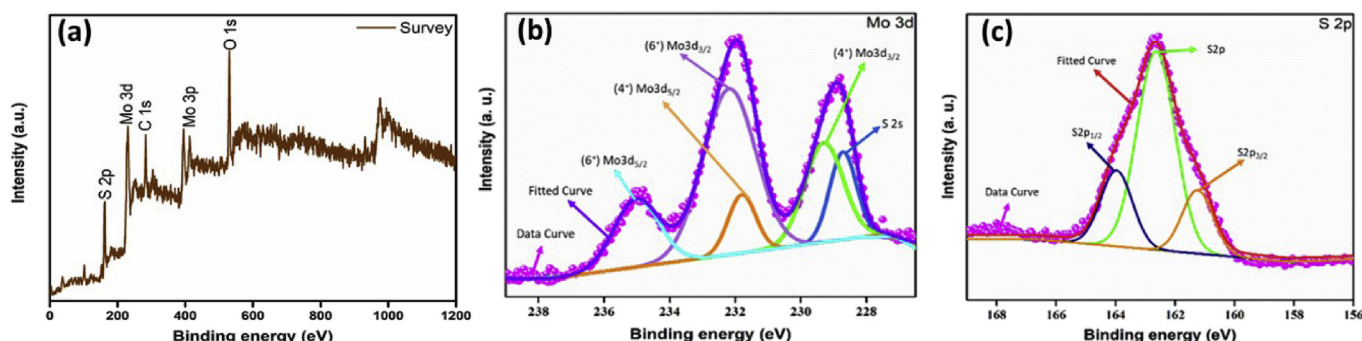

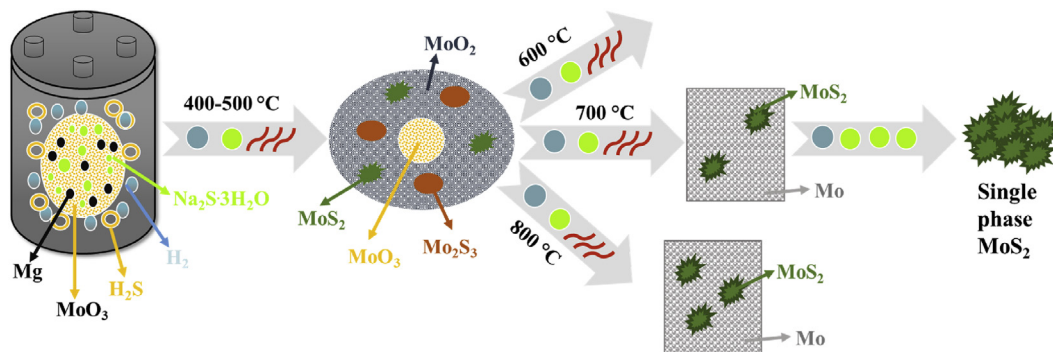**Fig. 7.** XPS spectrum of MS-11 (a) survey spectrum, (b) HR spectra of Mo 3d and (c) HR spectra of S 2p.

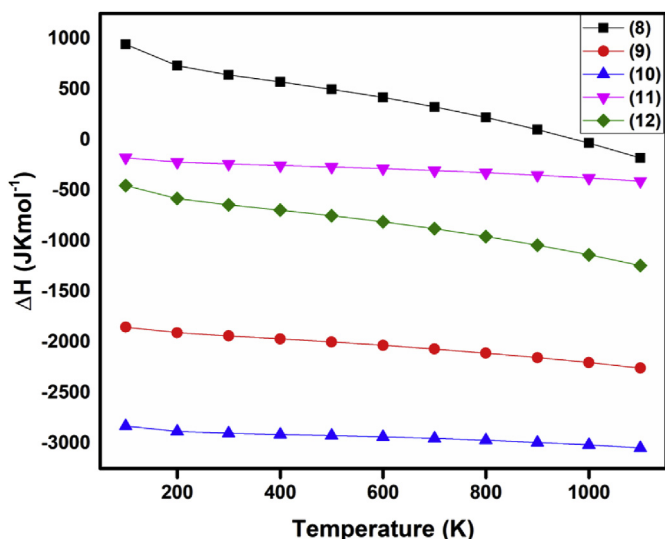**Fig. 8.** Schematic representation of synthesis of single phase nano molybdenum disulphide.
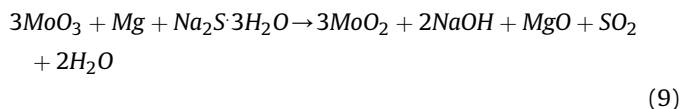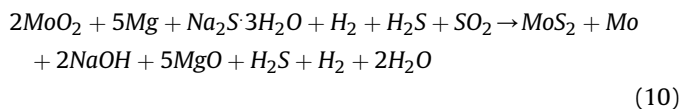

Fig. 9. Variation in heat of formation (ΔH) with temperature (K) for reactions (8)–(12).

$$3MoO_3 + Mg + Na_2S \cdot 3H_2O \rightarrow 3MoO_2 + 2NaOH + MgO + SO_2$$
$$+ 2H_2O$$

$$(9)$$

The reaction (Equation (9)) is the most favorable path for reduction of MoO_3 to MoO_2 among all the reaction paths represented in equations S7-S12 (SI). The variation of ΔH with temperature for (Equations S7-S12) formation of MoO_2 is given in Fig. S4 (S). However, no sulphurization has been considered till this reduction. Now, the evolved gases (H_2/H_2S) will further react to sulphurize MoO_2 to form MoS_2.

Increasing the temperature to 600−800 °C, the XRD analysis showed presence of both Mo and MoS_2 phases as indicated in Fig. 1. The possible reactions, for products synthesized at temperatures 600, 700 and 800 °C, based on thermodynamic kinetics for the transformation of MoO_2 to MoS_2 and Mo in presence of Mg and $Na_2S \cdot 3H_2O$ are listed in equation S13-S18 (SI). The most feasible reaction (10) is given below. The variation in heat of formation for this reaction with respect to change in temperature is shown in Fig. 9 and for other feasible reactions (equation S13-S18) is given in Fig. S5 (SI).

$$2MoO_2 + 5Mg + Na_2S \cdot 3H_2O + H_2 + H_2S + SO_2 \rightarrow MoS_2 + Mo$$
$$+ 2NaOH + 5MgO + H_2S + H_2 + 2H_2O$$

$$(10)$$

For complete sulphurization, sulphur content was increased. The feasible reactions at 700 °C (700 + 273 K) for sulphurization of Mo to MoS_2 has also been listed in equation S19-S20 (SI) with the most feasible pathway written in eq. (11).

$$Mo + SO_2 + Mg + Na_2S \cdot 3H_2O \rightarrow MoS_2 + MgO + 2NaOH + 2H_2O$$

$$(11)$$
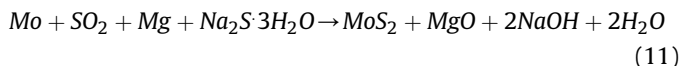
The plot of ΔH with respect to temperature for reaction (equation (11)) and equation S19-S20 (SI) are shown in Fig. 9 and Fig. S6 (SI), respectively. Whereas, as per the XRD analysis, the direct formation of pure phase MoS_2 is also possible inside the autoclave, if the adequate amount of sulphur is present. The feasibility of such transformation could occur through a number of possible reactions given in equations S21-S26 (SI). The most feasible path is given in equation (12) and the corresponding variation in ΔH with temperature is shown in Fig. 9. The plot of ΔH with temperature for reaction paths S21-S26 is given in Fig. S7 (SI).

$$MoO_3 + Mg + 3Na_2S \cdot 3H_2O \rightarrow MoS_2 + 6NaOH + MgO + 3H_2$$
$$+ 3H_2O$$

$$(12)$$
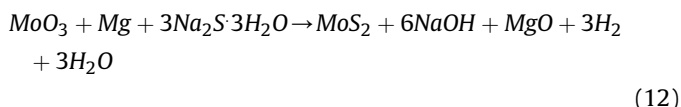
The reaction (12) seems to be most favorable transformation of MoO_3 to MoS_2 in presence of Mg, $Na_2S \cdot 3H_2O$. The pressure generated inside the autoclave also facilitate it. The schematic representation of the synthesis mechanism as discussed above is shown in Fig. 8.

3.10. Electrochemical studies

3.10.1. Hydrogen evolution reaction (HER) performance

The electrocatalytic performance of the synthesized MoS_2 nanostructures was investigated in both 0.5 M H_2SO_4 and 0.5 M KOH. The polarization curve of MS-11 obtained initially in acidic medium via linear sweep voltammetry (LSV) is shown in Fig. 10 (a), which shows maximum current density of 27.2 mAcm^{-2} at a potential of −0.6 V. However, the LSV curve of MS-13 in acidic medium shows the maximum current density of ∼30 mAcm^{-2} as shown in Fig. 10 (a). The enhanced current density is due to the highly crystalline phase of MoS_2, which enhances the surface characteristics. The results show enhanced current density value as compared to MoS_2 sheets, MoS_2 QD and bulk MoS_2 [53]. The stability is an important factor for a better performance and efficiency of electrocatalyst, which is the need of the present time. The stability of the synthesized MoS_2 nano structures has been investigated by performing cyclic voltammetry (CV) for 1000 cycles at a scan rate of 100 mVs^{-1} in the voltage window of (0.3 to −0.3 V). The polarization curves for both MS-11 and MS-13 obtained after 1000
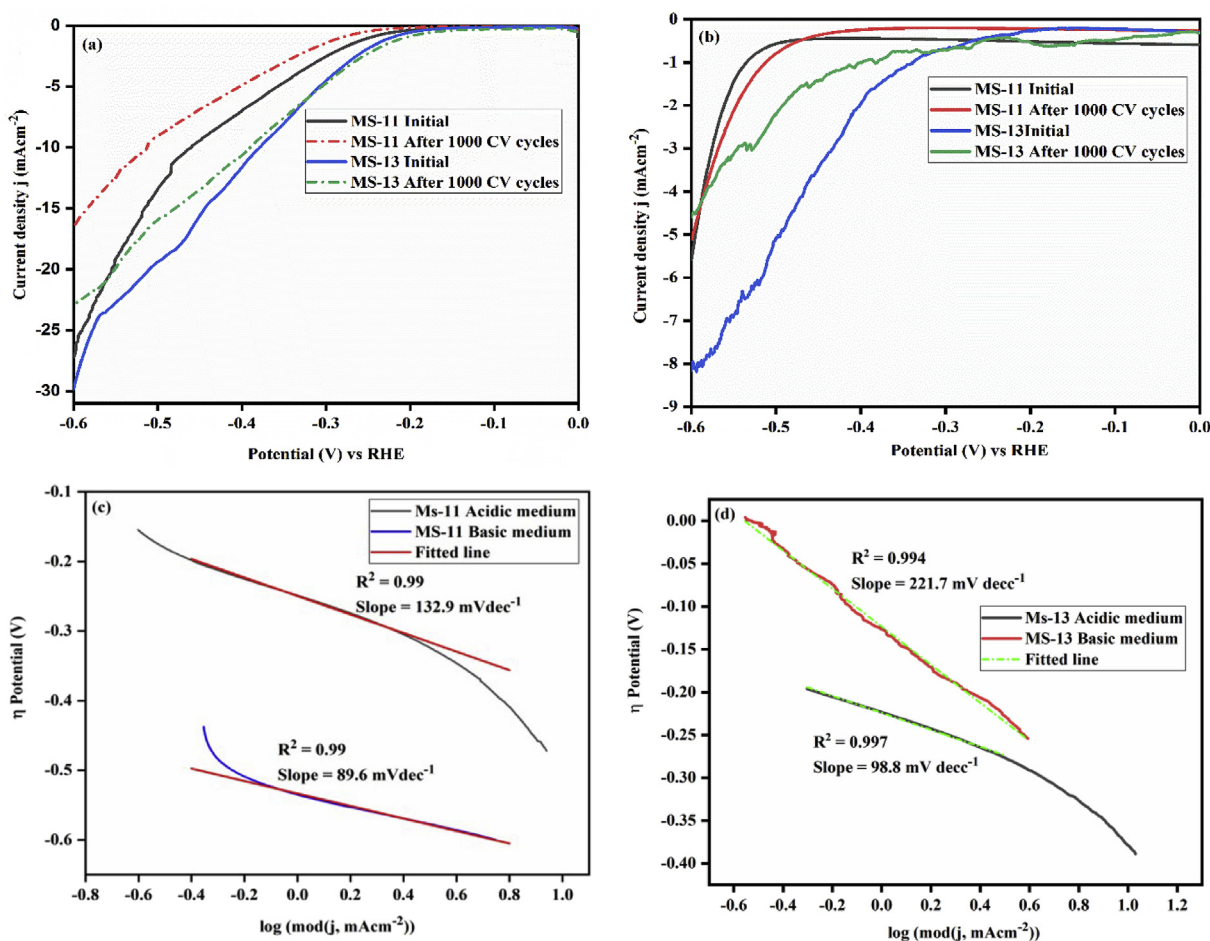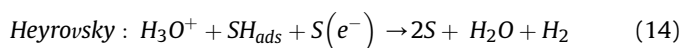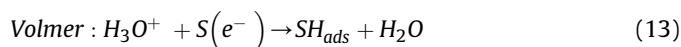
Fig. 10. **(a)** Linear sweep voltammetry (LSV) of MS-11 in acidic (0.5M H_2SO_4) and basic (0.5M KOH) medium, **(b)** LSV plots of MS-13 in acidic and basic medium, **(c)** Tafel slope for MS-11 in acidic and basic medium and **(d)** Tafel slope of MS-13 in acidic and basic medium.

CV cycles (Fig. 10 (a)) shows the LSV plot with loss of current by ~37 and 45%, respectively. The LSV plot of MS-11 (MoS_2) before and after 1000 CV cycles shows more stability in comparison to that obtained by Lin et al. [54]. The lower stability of MS-13 in comparison to MS-11 in the acidic medium could be the result of corrosion prone Mo and less electrochemical active MoO_2 phases. The LSV analysis shows that the synthesized material is a suitable and stable electrocatalyst for HER.

The LSV performed in basic medium represented in Fig. 10 (b) shows less amount of current density as compared to that of the acidic medium. The initial LSV in basic medium for both MS-11 and MS-13 shows the maximum current density of ~5.6 and 8.2 mAcm^{-2} respectively, which is very less as compared to that of acidic medium. The LSV curve performed after 1000 CV cycles at a scan rate of 100 mVs^{-1} shows a similar curve with negligible loss of current for MS-11 as shown in Fig. 10 (b). However, the MS-13 (Fig. 10 (b)) deteriorates in performance in the basic medium in same potential range. The higher amount of current in the acidic medium could be due to more H$^+$ ion production. This also reveals the higher amount of electrons produced on edge sites of MoS_2 in the acidic medium than that on surface in alkaline medium [55]. Moreover, the higher stability tested via CV shows higher stability in the basic medium, which attributes to oxidation resistance of MoS_2 and production of low sulphur ions [56].

Tafel plot is an important analysis to demonstrate the mechanism responsible for HER and electrocatalytic activity [57]. The

probable mechanism responsible for HER activity is predicted according to the following steps:

$$Volmer : H_3O^+ + S\left(e^-\right) \rightarrow SH_{ads} + H_2O \qquad (13)$$

$$Heyrovsky : H_3O^+ + SH_{ads} + S\left(e^-\right) \rightarrow 2S + H_2O + H_2 \qquad (14)$$

$$Tafel : 2S_{ads} \rightarrow 2S + H_2 \qquad (15)$$

Where S represents an active site of the species and SH_{ads} determines an H adsorbed intermediate. The HER takes place either by Volmer-Heyrovsky or Volmer-Tafel reaction. If the value of Tafel slope estimated from Tafel plot is close to 120 mVdec^{-1}, the reaction takes place by the combination of Volmer-Heyrovsky reaction steps. The value of Tafel slope near to 30 mVdec^{-1} shows Volmer-Tafel combination as the rate determining steps for HER. The smaller value of the Tafel slope depicts the enhanced reaction rate with respect to the given potential [57].

The Tafel plot for synthesized MoS_2 (MS-11) and MS-13 in acidic and alkaline medium is shown in Fig. 10 (c and d). The Tafel slope for MS-11 calculated via the linear fit of Tafel plot (Fig. 10 (c)) shows the value of 132.9 and 89.6 mVdec^{-1} in acidic and alkaline medium, respectively. The results determine Volmer reaction as the rate determining step for HER in an acidic electrolyte. However, the combination of Volmer-Heyrovsky determines the rate
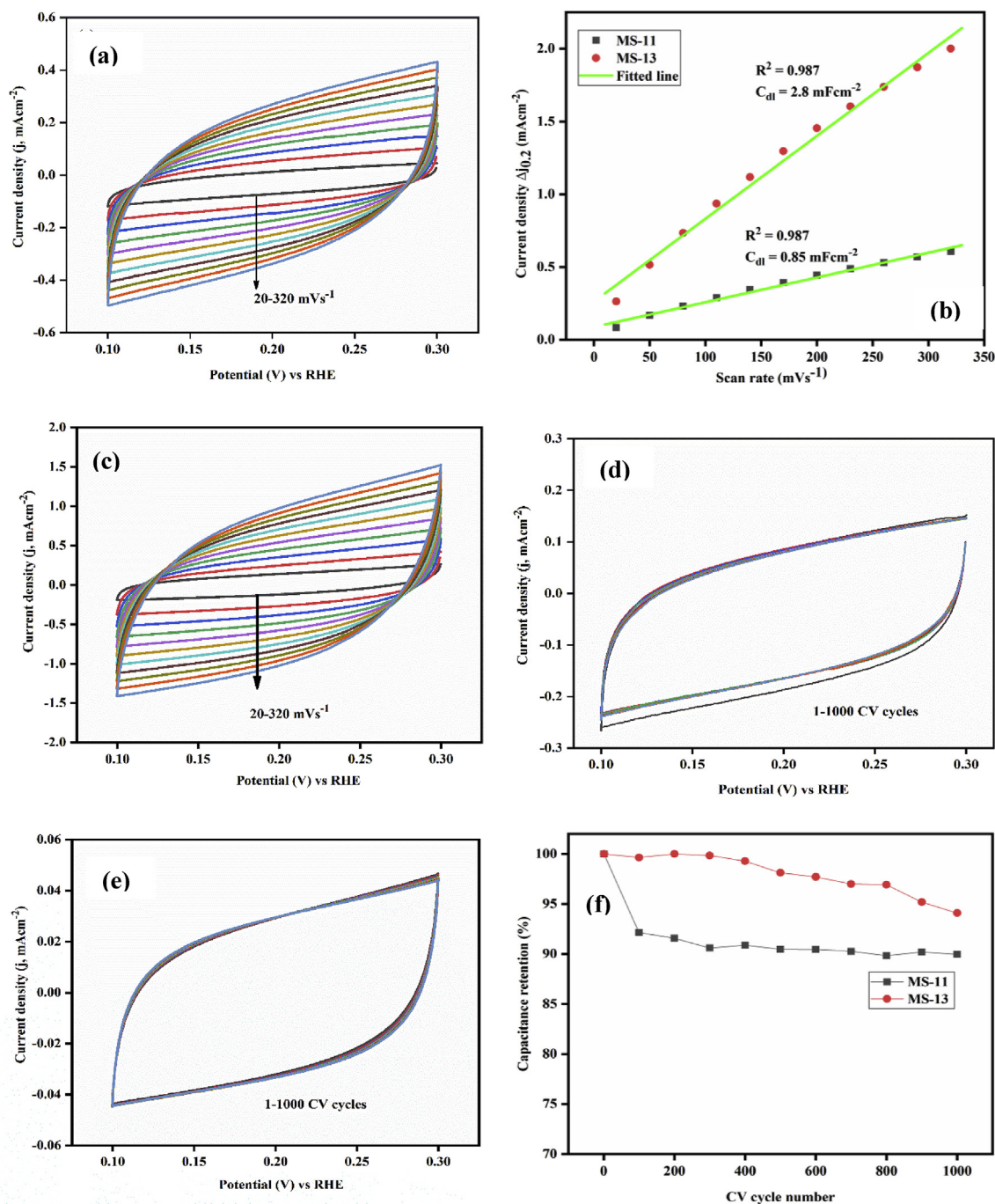
Fig. 11. **(a)** Cyclic voltammetry (CV) plots of MS-11 at multiple scan rates in acidic medium, **(b)** electric double layer capacitance (EDLC) of MS-11 and MS-13 in acidic medium, **(c)** CV plots of MS-13 at different scan rates in acidic medium, **(d)** and (e) CV plots for 1000 cycles of MS-11 and MS-13 in acidic medium and **(f)** capacitance retention with number of cycles in acidic medium.

determining step for HER in the basic electrolyte. The higher value of Tafel slope in acidic medium attributes to strong adsorption of H atom at the active site, which makes the discharge step difficult. However, the Tafel slope of MS-13 (Fig. 10 (d)) in acidic and basic electrolyte shows values of 98.8 and 221.7 mVdec^{-1}. The Tafel slope of MS-13 is lower in the basic medium, which attributes to different surface characteristics exhibited by highly crystalline phase and presence of some impure phase within the synthesized product. Moreover, the lower Tafel slope of MS-11 compared to MS-13 shows the faster charge transfer kinetics of the pure phase MoS$_2$. The

number of layers predicted by Raman spectroscopy is 5–6, which shows material characteristics is proceeding towards bulk; having the number of layers more than seven [16]. The bulk MoS$_2$ is one of the less electrochemical active species [53]. The higher Tafel slope of MoS$_2$ in acidic medium reveals a lesser number of vacant sites on edges of the MoS$_2$ layer, which enhances charge transfer kinetics. In acidic medium usually, the edge sites of MoS$_2$ are active species for HER, while as surface/terrace are responsible for HER in the basic medium [55]. The lower value of Tafel slope for MoS$_2$ in basic medium shows that the surface characteristics play the key role for

faster charge transfer kinetics. The inter-particle contact is very essential for HER activity, this could be the reason that MoS_2 is mostly used as co-catalyst for HER and electrode reactions [58]. The higher stability of MoS_2 in both in acidic and alkaline solutions and faster charge transfer kinetics on the surface other than the edges of the synthesized product makes it the suitable supportive catalyst for HER.

3.10.2. Double layer capacitance (C_{dl})

The electric double layer capacitance (EDLC, C_{dl}) has been evaluated from CV plots performed in acidic medium at various scan rates (20-320 mVs^{-1}) in the voltage range (0.1–0.3 V). The CV plot of MS-11 performed at multiple scan rates is shown in Fig. 11 (a). The nearly rectangular shape of CV plot determines the good reversibility of the material in the given voltage range. The C_{dl} value calculated from the plot of scan rate on x-axis vs $J_{0.2}$ on the y-axis is 0.85 mFcm^{-2} as shown in Fig. 11 (b). The CV plot versus scan rate for MS-13 is shown in Fig. 11 (c) and the corresponding C_{dl} so obtained is 2.8 mFcm^{-2} as given in Fig. 11 (b). The Cdl value of MS-13 is 3.3 times as that of MS-11, which again signifies the higher active surface sites in highly crystallized phase. The higher C_{dl} value of MS-13 compared to MS-11 may also contribute to the difference in sulphur orientations at the edge sites in highly crystalline nature of the synthesized material. The capacitance retention was tested via CV analysis performed at fix scan rate (100 mVs^{-1}) for 1000 CV cycles in the voltage range (0.1–0.3 V) in acidic medium for MS-11 and MS-13 as shown in Fig. 11 (d) and (e), respectively. The CV plot shape is retained even after 1000 cycles in both cases as shown in Fig. 12 (d) and (e). The plot of percentage capacitance retention with CV cycle number is shown in Fig. 12 (f). This shows enhanced capacitance retention in acidic medium. The only difference is observed for the first CV cycle, which shows little deviation from others on the lower side as shown in Fig. 12 (d), which remains same thereafter for all the CV cycles. The results also confirm the synthesized material a suitable electrode material for capacitor applications in acidic medium.

The CV plots performed at multiple scan rates (20-320 mVs^{-1}) in the voltage window 0.55–0.65 V for sample MS-11 in the basic medium is shown in Fig. S8 (a), (SI). The C_{dl} value obtained from the plot (Fig. S8 (b), SI) scan rate (x-axis) vs $J_{0.6}$ (y-axis) is 0.104 mFcm^{-2}. The CV plots of MS-13 performed at different scan rates in the similar voltage window reveals almost the similar C_{dl} value of 0.107 mFcm^{-2} (Fig. S8 (b), SI). The CV curves obtained in both MS-11 and MS-13 in basic medium are rectangular in shape, which signifies the higher electrochemical reversibility in charge/discharge process. The similar C_{dl} value of MS-11 and MS-13 in basic medium shows the similar surface activity with respect to scan rate. The capacitance retention of MS-11 and MS-13 in basic electrolyte was tested for 1000 CV cycles as shown in Fig. S8 (d) and (e), respectively. The capacitance retention plot with CV cycle number is shown in Fig. S8 (f). The higher difference is observed in the first CV cycle shape, which remains the same thereafter. However, in the present study, the ambiguous CV shape in the basic medium has been observed. To check the ambiguity the CV plots for MS-11 in alkaline medium, the CV analysis was done in the different voltage range (0.47–0.57 V) at various scan rates is shown in Fig. S9 (a), SI. The C_{dl} value calculated from the plot of scan rate (x-axis) vs $J_{0.52}$ (y-axis) is 1.20 mFcm^{-2} as shown in Fig. S9 (b), SI. The C_{dl} values obtained in alkaline medium is higher as compared to that obtained in acidic medium and is voltage dependent.

The value of C_{dl} is higher in the acidic medium compared to the basic electrolyte and is the surface characteristics of the material. However, the C_{dl} value of MS-11 is higher in basic medium. The higher values of C_{dl} obtained in acidic shows the synthesized material a potential candidate for capacitor and super-capacitor applications, which is the need of the present era. The comparison of the results obtained in acidic and alkaline medium determines the increase in the number of layers diminishes the electrocatalytic activity of the synthesized MoS_2 nanostructures.

4. Conclusion

Molybdenum disulphide (MoS_2) structures were successfully synthesized via reduction-sulphurization method in an autoclave at 700 °C for 10 h. The reaction temperature, reaction time and amount of sulphur content adherently affect the pure phase formation of MoS_2. Based on reaction kinetics and structural studies, a formation mechanism from MoO_3 to MoS_2 in an autoclave has been predicted. The FESEM studies reveal the agglomeration of synthesized powders and TEM/HRTEM shows the agglomeration in nano layered growth of hexagonal MoS_2 phase. The Raman spectroscopy reveals the formation of 5–6 layers of MoS_2. The optical properties studied by UV–Vis spectroscopy shows the presence of direct bandgap (2.29 eV). The photoluminescence spectra exhibit emission of blue and green color, when excited in UV-region. The synthesized MoS_2 nanostructures are highly stable electrocatalyst for HER in both acidic and alkaline medium. The EDLC shows MOS_2 as the potential electrode material for super-capacitors and batteries in an acidic electrolyte. The optical and electrochemical studies predict the broad application of synthesized MoS_2 in optoelectronic devices and gas/biosensors.

Novelty statement

Facile route of synthesis has been developed to get nano layered molybdenum disulphide (MoS_2) having 5 to 6 layers. The formation mechanism has been discussed in detail. The electrochemical studies reveal higher stability of MoS_2 in both acidic and basic medium showing higher capacitance retention.

Acknowledgment

Appendix A. Supplementary data

Supplementary data to this article can be found online at https://doi.org/10.1016/j.jallcom.2018.12.145.

References

[1] M. Chhowalla, H.S. Shin, G. Eda, L.J. Li, K.P. Loh, H. Zhang, The chemistry of two-dimensional layered transition metal dichalcogenide nanosheets, Nat. Chem. 5 (2013) 263–275, https://doi.org/10.1038/nchem.1589.
[2] R. Ganatra, Q. Zhang, Few-layer MoS2 : a promising layered semiconductor, ACS Nano 8 (2014) 4074–4099, https://doi.org/10.1021/nn405938z.
[3] H. Yuan, L. Kong, T. Li, Q. Zhang, A review of transition metal chalcogenide/graphene nanocomposites for energy storage and conversion, Chin. Chem. Lett. 28 (2017) 2180–2194, https://doi.org/10.1016/j.cclet.2017.11.038.
[4] K. Shomalian, M.M. Bagheri-Mohagheghi, M. Ardyanian, Synthesis and characterization of porous nanoparticles of molybdenum sulfide (MoS2) chalcogenide semiconductor prepared by polymerizing-complexing sol–gel method, J. Mater. Sci. Mater. Electron. 28 (2017) 14331–14340, https://doi.org/10.1007/s10854-017-7293-8.
[5] Q. Liu, X. Li, Q. He, A. Khalil, D. Liu, T. Xiang, X. Wu, L. Song, Gram-scale Aqueous synthesis of stable few-layered 1T-MoS2: applications for visible-light-driven photocatalytic hydrogen evolution, Small 11 (2015) 5556–5564, https://doi.org/10.1002/smll.201501822.
[6] X. Xu, W. Liu, Y. Kim, J. Cho, Nanostructured transition metal sulfides for lithium ion batteries: progress and challenges, Nano Today 9 (2014) 604–630,

https://doi.org/10.1016/j.nantod.2014.09.005.

[7] U. Krishnan, M. Kaur, G. Kaur, K. Singh, A.R. Dogra, M. Kumar, A. Kumar, MoS2/ZnO nanocomposites for efficient photocatalytic degradation of industrial pollutants, Mater. Res. Bull. 111 (2019) 212–221, https://doi.org/10.1016/j.materresbull.2018.11.029.

[8] S.A. Han, R. Bhatia, S.-W. Kim, Synthesis, properties and potential applications of two-dimensional transition metal dichalcogenides, Nano Converg. 2 (2015) 17, https://doi.org/10.1186/s40580-015-0048-4.

[9] A. Gupta, T. Sakthivel, S. Seal, Recent development in 2D materials beyond graphene, Prog. Mater. Sci. 73 (2015) 44–126, https://doi.org/10.1016/j.pmatsci.2015.02.002.

[10] Q.H. Wang, K. Kalantar-Zadeh, A. Kis, J.N. Coleman, M.S. Strano, Electronics and optoelectronics of two-dimensional transition metal dichalcogenides, Nat. Nanotechnol. 7 (2012) 699–712, https://doi.org/10.1038/nnano.2012.193.

[11] Z. He, W. Que, Molybdenum disulfide nanomaterials: structures, properties, synthesis and recent progress on hydrogen evolution reaction, Appl. Mater. Today 3 (2016) 23–56, https://doi.org/10.1016/j.apmt.2016.02.001.

[12] X.L. Yin, L.L. Li, W.J. Jiang, Y. Zhang, X. Zhang, L.J. Wan, J.S. Hu, MoS2/CdS nanosheets-on-nanorod heterostructure for highly efficient photocatalytic H-2 generation under visible light irradiation, ACS Appl. Mater. Interfaces 8 (2016) 15258–15266, https://doi.org/10.1021/acsami.6b02687.

[13] J. Sun, L. Duan, Q. Wu, W. Yao, Synthesis of MoS2quantum dots cocatalysts and their efficient photocatalytic performance for hydrogen evolution, Chem. Eng. J. 332 (2018) 449–455, https://doi.org/10.1016/j.cej.2017.09.026.

[14] B. Sun, F. Shan, X. Jiang, J. Ji, F. Wang, One-pot synthesis of MoS2/In2S3ultrathin nanoflakes with mesh−shaped structure on indium tin oxide as photocathode for enhanced photo-and electrochemical hydrogen evolution reaction, Appl. Surf. Sci. 435 (2018) 822–831, https://doi.org/10.1016/j.apsusc.2017.11.065.

[15] B. Han, Y.H. Hu, MoS 2 as a co-catalyst for photocatalytic hydrogen production from water, Energy Sci. Eng. 4 (2016) 285–304, https://doi.org/10.1002/ese3.128.

[16] A. Splendiani, L. Sun, Y. Zhang, T. Li, J. Kim, C.Y. Chim, G. Galli, F. Wang, Emerging photoluminescence in monolayer MoS2, Nano Lett. 10 (2010) 1271–1275, https://doi.org/10.1021/nl903868w.

[17] G. Eda, H. Yamaguchi, D. Voiry, T. Fujita, M. Chen, M. Chhowalla, Supporting information for "photoluminescence from chemically exfoliated MoS2", Nano Lett. 11 (2011) 5111–5116, https://doi.org/10.1021/nl201874w.

[18] X. Zhang, Z. Lai, C. Tan, H. Zhang, Solution-processed two-dimensional MoS2Nanosheets: preparation, hybridization, and applications, Angew. Chem. Int. Ed. 55 (2016) 8816–8838, https://doi.org/10.1002/anie.201509933.

[19] K. Chang, W. Chen, In situ synthesis of MoS2/graphene nanosheet composites with extraordinarily high electrochemical performance for lithium ion batteries, Chem. Commun. 47 (2011) 4252–4254, https://doi.org/10.1039/c1cc10631g.

[20] Y. Yan, X. Ge, Z. Liu, J.Y. Wang, J.M. Lee, X. Wang, Facile synthesis of low crystalline MoS2 nanosheet-coated CNTs for enhanced hydrogen evolution reaction, Nanoscale 5 (2013) 7768–7771, https://doi.org/10.1039/c3nr02994h.

[21] M.A. Lukowski, A.S. Daniel, F. Meng, A. Forticaux, L. Li, S. Jin, Enhanced hydrogen evolution catalysis from chemically exfoliated metallic MoS2 nanosheets, J. Am. Chem. Soc. 135 (2013) 10274–10277, https://doi.org/10.1021/ja404523s.

[22] Z. Wang, B. Mi, Environmental applications of 2D molybdenum disulfide (MoS2) nanosheets, Environ. Sci. Technol. 51 (2017) 8229–8244, https://doi.org/10.1021/acs.est.7b01466.

[23] A.B. Laursen, S. Kegnæs, S. Dahl, I. Chorkendorff, Molybdenum sulfides—efficient and viable materials for electro - and photoelectrocatalytic hydrogen evolution, Energy Environ. Sci. 5 (2012) 5577, https://doi.org/10.1039/c2ee02618j.

[24] H. Lin, X. Chen, H. Li, M. Yang, Y. Qi, Hydrothermal synthesis and characterization of MoS2 nanorods, Mater. Lett. 64 (2010) 1748–1750, https://doi.org/10.1016/j.matlet.2010.04.032.

[25] B. Dong, Y.M. Chai, Y.Q. Liu, C.G. Liu, Hydrothermal synthesis and characterization of novel MoS2 nanoflowers directed by Ionic liquid, Adv. Eng. Mater. 194–196 (Pts 1–3) (2011) 785–789, 10.4028/www.scientific.net/AMR.194-196.785.

[26] X. Wang, Z. Zhang, Y. Chen, Y. Qu, Y. Lai, J. Li, Morphology-controlled synthesis of MoS2nanostructures with different lithium storage properties, J. Alloys Compd. 600 (2014) 84–90, https://doi.org/10.1016/j.jallcom.2014.02.127.

[27] A.J. Cheah, W.S. Chiu, P.S. Khiew, S. Radiman, M.A.A. Hamid, Synthesis and characterization of visible-active molybdenum disulfide (2H-MoS2) nanospheres, AIP Conf. Proc. 1669 (2015), 020030, https://doi.org/10.1063/1.4919168.

[28] H. Yang, J. Zhao, C. Wu, C. Ye, D. Zou, S. Wang, Facile synthesis of colloidal stable MoS2nanoparticles for combined tumor therapy, Chem. Eng. J. 351 (2018) 548–558, https://doi.org/10.1016/j.cej.2018.06.100.

[29] C.H. Ravikumar, G.V. Nair, S. Muralikrishna, D.H. Nagaraju, R.G. Balakrishna, Nanoflower like structures of MoSe2and MoS2as efficient catalysts for hydrogen evolution, Mater. Lett. 220 (2018) 133–135, https://doi.org/10.1016/j.matlet.2018.03.012.

[30] M.F. Afsar, M.A. Rafiq, S. Fizza, F. Saira, M.M. Chaudhary, M.M. Hasan, A.I.Y. Tok, Two-dimensional Molybdenum disulphide nanoflakes synthesized by liquid-solid phase reaction method: regenerative photocatalytic

performance under UV-visible light irradiation by advance oxidation process, Mater. Res. Express 5 (2018), 056206, https://doi.org/10.1016/j.jhazmat.2007.08.020.

[31] H. Singh, O.P. Pandey, Novel process for synthesis of nanocrystalline WC from wolframite ore, Ceram. Int. (2015), https://doi.org/10.1016/j.ceramint.2015.04.135.

[32] R.A. Mir, P. Sharma, O.P. Pandey, Thermal and structural studies of carbon coated Mo2C synthesized via in-situ single step reduction-carburization, Sci. Rep. 7 (2017) 3518, https://doi.org/10.1038/s41598-017-03197-8.

[33] J.M. Zhang, Y. Zhang, K.W. Xu, V. Ji, Anisotropic elasticity in hexagonal crystals, Thin Solid Films 515 (2007) 7020–7024, https://doi.org/10.1016/j.tsf.2007.01.045.

[34] Y. Li, R.B. Thompson, Relations between elastic constants C_{ij} and texture parameters for hexagonal materials, J. Appl. Phys. 67 (1990) 2663–2665, https://doi.org/10.1063/1.345479.

[35] R. López, R. Gómez, Band-gap energy estimation from diffuse reflectance measurements on sol-gel and commercial TiO2: a comparative study, J. Sol Gel Sci. Technol. 61 (2012) 1–7, https://doi.org/10.1007/s10971-011-2582-9.

[36] L. Brewer, R.H. Lamoreaux, The Mo-S system (Molybdenum-Sulfur), Bull. Alloy Phase Diagrams 1 (1980) 93–95, https://doi.org/10.1007/BF02881201.

[37] G. Li, C. Li, H. Tang, K. Cao, J. Chen, F. Wang, Y. Jin, Synthesis and characterization of hollow MoS2microspheres grown from MoO3 precursors, J. Alloys Compd. 501 (2010) 275–281, https://doi.org/10.1016/j.jallcom.2010.04.088.

[38] X.-L. Li, Y.-D. Li, MoS2 nanostructures: synthesis and electrochemical Mg2+ intercalation, J. Phys. Chem. B 108 (2004) 13893–13900, https://doi.org/10.1021/jp0367575.

[39] B. Sheng, J. Liu, Z. Li, M. Wang, K. Zhu, J. Qiu, J. Wang, Effects of excess sulfur source on the formation and photocatalytic properties of flower-like MoS2-spheres by hydrothermal synthesis, Mater. Lett. 144 (2015) 153–156, https://doi.org/10.1016/j.matlet.2015.01.056.

[40] A.V. Kolobov, J. Tominaga, Two-dimensional Transition-metal Dichalcogenides, 2016, https://doi.org/10.1007/978-3-319-31450-1.

[41] A. Castellanos-Gomez, M. Poot, G.A. Steele, H.S.J. Van Der Zant, N. Agrait, G. Rubio-Bollinger, Elastic properties of freely suspended MoS 2 nanosheets, Adv. Mater. 24 (2012) 772–775, https://doi.org/10.1002/adma.201103965.

[42] H. Li, Q. Zhang, C.C.R. Yap, B.K. Tay, T.H.T. Edwin, A. Olivier, D. Baillargeat, From bulk to monolayer MoS2: evolution of Raman scattering, Adv. Funct. Mater. 22 (2012) 1385–1390, https://doi.org/10.1002/adfm.201102111.

[43] A.K. Mishra, K.V. Lakshmi, L. Huang, Eco-friendly synthesis of metal dichalcogenides nanosheets and their environmental remediation potential driven by visible light, Sci. Rep. 5 (2015) 1–8, https://doi.org/10.1038/srep15718.

[44] C. Lee, H. Yan, L. Brus, T. Heinz, J. Hone, S. Ryu, Anomalous lattice vibrations of single-and few-layer MoS2, ACS Nano 4 (2010) 2695–2700, https://doi.org/10.1021/nn1003937.

[45] G.L. Frey, S. Elani, M. Homyonfer, Y. Feldman, R. Tenne, Optical-absorption spectra of inorganic fullerenelike MS2 (M = Mo, W), Phys. Rev. B 57 (1998) 6666–6671, https://doi.org/10.1103/PhysRevB.57.6666.

[46] J.Z. Ou, A.F. Chrimes, Y. Wang, S.Y. Tang, M.S. Strano, K. Kalantar-Zadeh, Ion-driven photoluminescence modulation of quasi-two-dimensional MoS 2 nanoflakes for applications in biological systems, Nano Lett. 14 (2014) 857–863, https://doi.org/10.1021/nl4042356.

[47] G. Eda, H. Yamaguchi, D. Voiry, T. Fujita, M. Chen, M. Chhowalla, Photoluminescence from chemically exfoliated MoS2, Nano Lett. 11 (2011) 5111–5116, https://doi.org/10.1021/nl201874w.

[48] M.D. Patel, J. Zhang, J. Park, N. Choudhary, J.M. Tour, W. Choi, Directly deposited porous two-dimensional MoS2films as electrocatalysts for hydrogen evolution reactions, Mater. Lett. 225 (2018) 65–68, https://doi.org/10.1016/j.matlet.2018.04.093.

[49] Z. Yang, D. Gao, J. Zhang, Q. Xu, S. Shi, K. Tao, D. Xue, Realization of high curie temperature ferromagnetism in atomically thin MoS2, WS2 nanosheets with uniform and flower−like morphology, Nanoscale 7 (2015) 650–658, https://doi.org/10.1039/C4NR06141A.

[50] H.K. Sidana, R.A. Mir, O.P. Pandey, Synthesis of molybdenum nitride (Mo2N) nanoflakes via in-situ reduction-nitridation, J. Alloys Compd. 736 (2018) 255–265, https://doi.org/10.1016/j.jallcom.2017.09.268.

[51] J. Dang, G.H. Zhang, K.C. Chou, R.G. Reddy, Y. He, Y. Sun, Kinetics and mechanism of hydrogen reduction of MoO3to MoO2, Int. J. Refract. Met. Hard Mater. 41 (2013) 216–223, https://doi.org/10.1016/j.ijrmhm.2013.04.002.

[52] J. Dang, G.-H. Zhang, K.-C. Chou, R.G. Reddy, Y. He, Y. Sun, Kinetics and mechanism of hydrogen reduction of MoO3 to MoO2, Int. J. Refract. Met. Hard Mater. 41 (2013) 216–223, https://doi.org/10.1016/j.ijrmhm.2013.04.002.

[53] S. Pal, K.K. Tadi, P.M. Sudeep, S. Radhakrishnan, T.N. Narayanan, Temperature assisted shear exfoliation of layered crystals for the large-scale synthesis of catalytically active luminescent quantum dots, Mater. Chem. Front. 1 (2017) 319–325, https://doi.org/10.1039/C6QM00081A.

[54] L. Ma, X. Zhou, L. Xu, C. Ye, J. Luo, X. Xu, L. Zhang, W. Chen, SDBS-assisted hydrothermal preparation and electrocatalytic properties of few-layer and edge-rich MoS2 nanospheres, Superlattices Microstruct. 83 (2015) 112–120, https://doi.org/10.1016/j.spmi.2015.03.031.

[55] J.D. Wiensch, J. John, J.M. Velazquez, D.A. Torelli, A.P. Pieterick, M.T. McDowell, K. Sun, X. Zhao, B.S. Brunschwig, N.S. Lewis, Comparative study in acidic and alkaline media of the effects of pH and crystallinity on the hydrogen-evolution reaction on MoS 2 and MoSe 2, ACS Energy Lett. 2 (2017) 2234–2238, https://doi.org/10.1021/acsenergylett.7b00700.

[56] Y.-H. Choi, J. Cho, A.M. Lunsford, M. Al-Hashimi, L. Fang, S. Banerjee, Mapping

the electrocatalytic activity of MoS$_2$ across its amorphous to crystalline transition, J. Mater. Chem. A. 5 (2017) 5129–5141, https://doi.org/10.1039/C6TA10316B.

[57] R.A. Mir, O.P. Pandey, Influence of graphitic/amorphous coated carbon on HER activity of low temperature synthesized β-Mo2C@C nanocomposites, Chem. Eng. J. 348 (2018) 1037–1048, https://doi.org/10.1016/j.cej.2018.05.041.

[58] Z. Xing, Q. Liu, A.M. Asiri, X. Sun, Closely interconnected network of molybdenum phosphide nanoparticles: a highly efficient electrocatalyst for generating hydrogen from water, Adv. Mater. 26 (2014) 5702–5707, https://doi.org/10.1002/adma.201401692.